Ambient-pressure superconductivity above 100 K in hole-doped carbon clathrates with superior hardness

Yu-Lin Han [1], Kai-Yue Jiang,[1] Bao-Tian Wang,[2,3] Ping Zhang,[1,4] and Hong-Yan Lu [1,*]

[1]*School of Physics and Physical Engineering, Qufu Normal University, Qufu 273165, China*
[2]*Institute of High Energy Physics, Chinese Academy of Sciences, Beijing 100049, China*
[3]*Spallation Neutron Source Science Center, Dongguan 523803, China*
[4]*Institute of Applied Physics and Computational Mathematics, Beijing 100088, China*

To explore phonon-mediated superconductors with critical temperature (T_c) exceeding the liquid-nitrogen temperature under ambient pressure, two pure carbon structures C_6 and C_{10} with a carbon-cage-network are designed and their superconductivity is investigated. By shifting the Fermi level by hole doping, we successfully obtain the metallized sp^3-hybridized covalent σ-bonding bands, which generally show strong coupling with phonons. Based on first-principles calculations and the Wannier interpolation technique, the lattice dynamics, mechanical properties, electronic structures, and electron-phonon coupling of hole-doped C_6 and C_{10} clathrates are investigated. Both the enlarged density of states at the Fermi level and the softened phonons play significant roles in the enhancement of electron-phonon coupling. By solving the anisotropic Eliashberg equations, we find that the T_c of hole-doped C_6 and C_{10} clathrates can reach about 43 K and 150 K, respectively. Additionally, pristine C_6 and C_{10} clathrates exhibit ultrahigh hardness simultaneously. This study suggests that a carbon-cage-network is another direction to explore materials simultaneously possessing high-temperature superconductivity and ultrahigh hardness.

I. INTRODUCTION

Since superconductivity was discovered by Onnes more than 110 years ago, boosting superconducting T_c has become one of the the most fascinating research topics in condensed matter physics. High T_c may be induced in the light-element compounds, owing to their high Debye temperature, which reflects the energy scale of electron pairing. Experimental evidence has confirmed the superconductivity of previously predicted dense sulfur hydride with $T_c \sim$ 203 K at 155 GPa [1,2], offering another route in the search for high-temperature superconductivity in conventional superconductors [3]. Binary hydrides remain the most promising system for fruitful synergy between theory and experiment. When hydrogen atoms form clathrate-like structures under high pressure, they can also exhibit extremely high T_c. For instance, 215 K in clathrate calcium hydride CaH_6 at 172 GPa [4,5] and the subsequently 224 K in YH_6 at 166 GPa [6,7] have been experimentally reported, with calcium and yttrium atoms located at the center of H_{24} cages. Clathrate-like structures with even greater hydrogen content were later predicted for rare-earth hydrides YH_{10}, LaH_{10}, and CeH_{10} [8,9]. The superconductivity has been experimentally confirmed to be $\sim$ 250–260 K in LaH_{10} at 170–180 GPa [10,11], and 115 K in CeH_{10} at 95 GPa [12], which are close to the predicted results. Based on the Bardeen-Cooper-Schrieffer (BCS) [13] and Migdal-Eliashberg theories [14], the high T_c of hydrogen-rich

superconductors markedly benefits from strong electron-phonon coupling (EPC) and high-frequency hydrogen-related phonons, which satisfies two of the three factors that affect the T_c of phonon-mediated superconductors, with the other one the high density of states (DOS) at the Fermi level $N(0)$ [15]. Although the clathrate structures formed by H atoms successfully drive the near room-temperature superconductivity, the condition of extremely high pressure to realize the T_c is challenging to achieve in general laboratories, and the decrease of pressure will lead to structural phase transition and the lost of stability, making hydrogen-based superconducting materials rather difficult in practical applications.

Since the near-room-temperature superconductivity of hydrides is almost exclusively present in certain special structures, such as the aforementioned cage configuration [4–12], whether these cagelike network can remain stable and superconducting at low or even ambient pressure is fascinating. However, the stability of the hydrogen cages mentioned above cannot be maintained under ambient pressure. Compared with hydrides, carbides are another widely concerned and investigated materials. It has been reported that when carbon atoms form a cagelike structure, they can successfully stabilize under ambient pressure. For instance, the best-known one is fullerene [16,17]. In the case of fullerene crystals, superconductivity has been discovered, and the T_c can be tuned in the range of 18–40 K in alkali-metal-doped C_{60} [18–20]. In some so-called smaller fullerenes, superconductivity has also been investigated, such as 55 K in Na-doped C_{20} [21]. In the halogen-doped carbon clathrate FC_{34}, with the coalescence of C_{20} and C_{28} cages, the T_c was theoretically predicted to be

*Contact author: hylu@qfnu.edu.cn

77 K [22], reaching the liquid nitrogen temperature. Additionally, the predicted T_c can be up to 80 K in metal-doped (BC)$_3$ clathrates [23–25]. Based on the above research, it can be seen that, unlike isolated-like fullerene crystals, high-T_c superconductivity turned out to be induced in the clathrate structures with strong bond coupling among carbon cluster units. One possible reason for the low T_c of isolated fullerene crystals may be the lack of strong structural coupling between clathrate units.

Here, employing the method of element replacement, we have designed two pure carbon clathrates, C$_6$ and C$_{10}$, inspired by the clathrate structures formed by H atoms in experimentally synthesized CaH$_6$ [4,5] and LaH$_{10}$ [9,11]. The structural design is based on the principle that carbon atoms form distinct cagelike features, with apparent coupling characteristics between the cage units, such as sp^3-hybridized σ bonds or shared atomic surfaces. First-principles calculations, in conjunction with the Wannier interpolation technique [26–29], are performed to determine the lattice dynamics, electronic structures, and superconductivity properties of C$_6$ and C$_{10}$ clathrates. The results indicate that the pristine C$_6$ and C$_{10}$ are both insulators but simultaneously exhibit ultra-high hardness. Interestingly, van Hove singularities (vHs) are observed in the DOS below the Fermi level. If these clathrates can be metallized to approach these singularities, high-T_c superconductivity may be induced since the enhanced DOS and high-frequency phonon conditions could be satisfied simultaneously. Additionally, previous investigations have illustrated that the σ-bonding bands exhibit a more pronounced reaction to lattice vibration in contrast to the π bands, which in turn exert a stronger impact on EPC [24,30–33], thereby also satisfying the third criterion.

In addition to the application of pressure, carrier doping stands out as another widely adopted strategy for the achievement of metallization. By doping holes, shifting the Fermi level downward, the sp^3-hybridization σ-bonding bands undergo metallization, thereby successfully inducing superconductivity in these carbon clathrates. Remarkably, without triggering obvious structural phase transitions, the strengths of EPC are determined to be 0.76 and 2.23 in hole-doped C$_6$ and C$_{10}$ clathrates, respectively. The enhanced EPC obtained in both clathrates can be attributed to the increased DOS and the softening of phonons. By solving the anisotropic Eliashberg equations [14], the strong EPC efficiently pairs electrons into high-T_c superconducting states. This results in maximum T_c of ~43 K and ~150 K for hole-doped C$_6$ and C$_{10}$, respectively. Moreover, through the analysis of mechanical properties, it is revealed that both clathrates exhibit excellent hardness, indicating that hole-doped C$_6$ and C$_{10}$ clathrates possess both high-T_c superconductivity and ultra-high hardness characteristics.

II. RESULTS AND DISCUSSION

A. Lattice structure, stability, and mechanical properties

The structural characteristics and stability of these carbon-cage networks are examined firstly. Figure 1 illustrates the optimized crystal structures of C$_6$ and C$_{10}$ clathrates. The carbon cages overlap and repeat in three crystal directions under the periodic conditions, forming a spatial ordered structure.
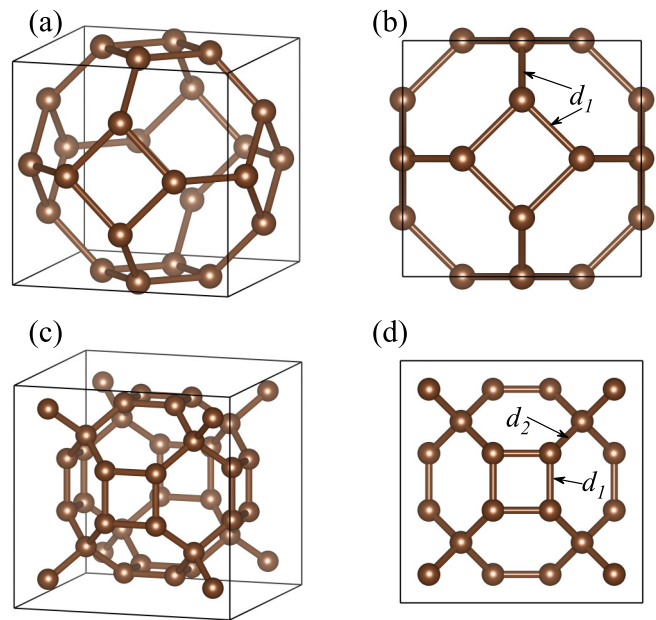
FIG. 1. Crystal structures of C$_6$ and C$_{10}$ clathrates. (a, c) Three-dimensional view; (b, d) view along the [100] direction.

Both carbon clathrates possess cubic symmetry with the space group of $Im\bar{3}m$ (No. 229) for C$_6$ and $Fm\bar{3}m$ (No. 225) for C$_{10}$. At ambient pressure, the optimized crystal lattice constants of C$_6$ and C$_{10}$ clathrates are 4.38 and 6.69 Å, respectively. In C$_6$, consisting of six squares and eight hexagons, seen in Figs. 1(a) and 1(b), the bond length between carbon atoms is uniform at 1.55 Å. Conversely, the structure of the carbon cage in C$_{10}$ exhibits slight differences, with six squares and twelve hexagons. Notably, the bond lengths between the carbon atoms in C$_{10}$ clathrates vary. Specifically, the bond length in the square [d_1 in Fig. 1(d)] is 1.58 Å, whereas the length of bonds shared by the hexagonal ring [d_2 in Fig. 1(d)] is 1.54 Å. The atomic distances in C$_6$ and C$_{10}$ clathrates closely resemble the nearest-neighbor C-C distance of diamond (1.54 Å) [34], graphene (1.42 Å) [35], and C-sodalite structures (1.53 Å), all of which are renowned for their exceptional stability.

To explore the chemical bonding nature of these carbon clathrates, the electron localization function (ELF) [36], which represents the normalized electron density and provides intuitive insight into the bonding characteristics between atoms, is plotted and shown in Fig. S2 of the Supplemental Material (SM) [37] (which also contains Refs. [38–58]). The results reveal that the localized function between carbon atoms within both C$_6$ and C$_{10}$ clathrates surpasses 0.9, and the larger value indicates stronger covalent binding [59], indicating that strong nonpolar covalent bonds are formed between carbon atoms through sp^3 hybridization. For more details, the calculated crystal orbital Hamiltonian population (COHP) [60] depicted in Fig. S3 [37] reveals fully occupied bonding states situated below the Fermi level, evidencing the formation of strong covalent C-C bonds within these carbon cages. The integrated COHP values between C-C pairs are −8.98 eV per bond in C$_6$, whereas in C$_{10}$, they stand at −8.23 and −9.79 eV per bond, respectively, arising from the distinct bond lengths
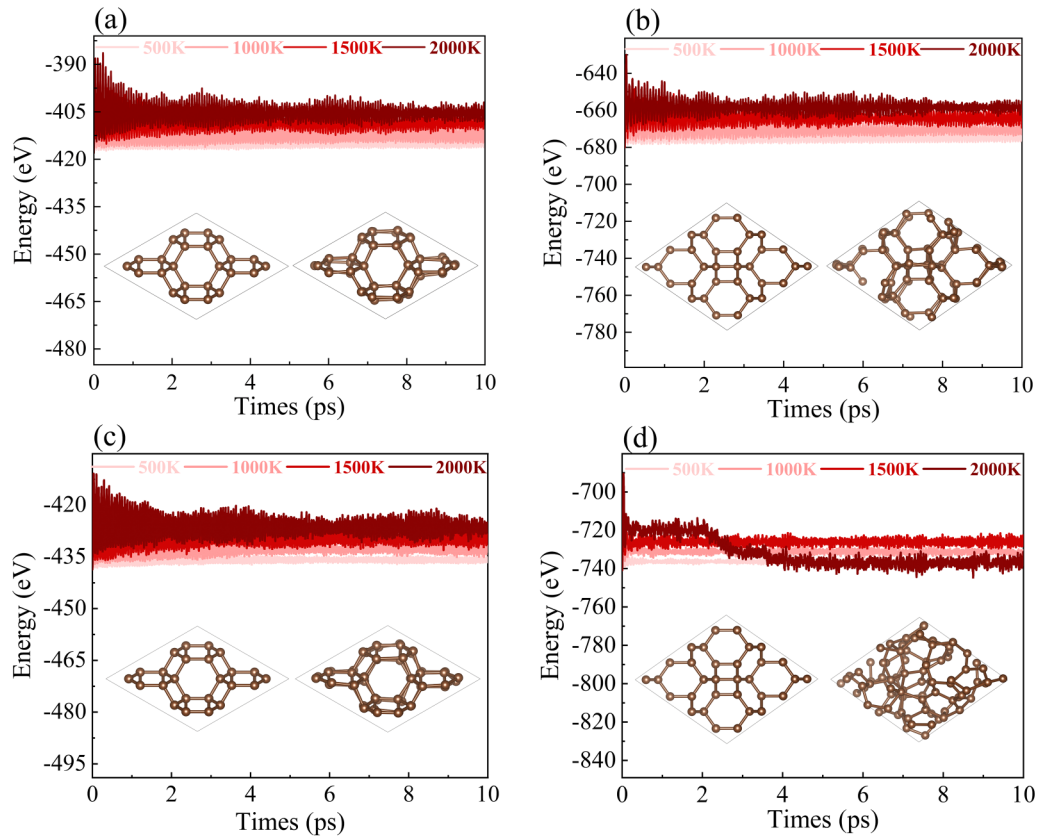
FIG. 2. Total energy of pristine (a, b) and hole-doped (c, d) C_6 and C_{10} clathrates vs simulation time at 500–2000 K. The insets are structure snapshots at 0 and 10 ps at the highest temperature of 2000 K.

between carbon atoms. Additionally, charge density difference is also conducted to aid the analysis. The accumulation of charges on these C-C bonds further enhances the strength of these covalent bonds, akin to those found in diamond, thereby endowing these clathrates with structural stability even in the absence of external pressure.

The absence of imaginary modes in the phonon dispersion spectra confirms the lattice dynamic stability of C_6 and C_{10}, as illustrated in Fig. S4 [37]. Moreover, ensuring thermodynamic stability is paramount for the practical application of these carbon-based clathrates. To better illustrate their thermal stability, the *ab initio* molecular dynamics (AIMD) simulations are conducted over a total simulation period of 10 ps, ranging from 500 to 2000 K. Figures 2(a) and 2(b) depict the fluctuation of total energies within these pristine carbon clathrates, in which no significant energy mutation is observed. Additionally, snapshots captured after 10 ps reveal that all atoms vibrate around their equilibrium sites, maintaining the basic structure even at 2000 K. For the hole-doped C_6 and C_{10} clathrates, the AIMD simulation results shown in Fig. 2(c) indicate that the energy of hole-doped C_6 does not undergo significant fluctuations at the high temperature of 2000 K. For hole-doped C_{10} [Fig. 2(d)], the energy exhibits a significant decrease at 2000 K after 2 ps, indicating that the hole-doped C_{10} undergoes a structural phase transition at 2000 K, but it still maintains well stability at 1500 K. Thus, the AIMD results confirm the robust thermodynamic stability for C_6 and C_{10} clathrates, in both pristine and doped cases.

Mechanical properties play a critical role in determining the practical applicability of materials. To gain a comprehensive understanding of the mechanical characteristics of these carbon clathrates, elastic constants (C_{ij}) are first examined, with the results listed in Table I. Both C_6 and C_{10} clathrates exhibit three independent elastic constants, which are C_{11}, C_{12}, and C_{44}. Generally, a mechanically stable material with cubic symmetry is expected to adhere to the Born criteria [61]: $C_{11} - C_{12} > 0$, $C_{11} + 2C_{12} > 0$, $C_{44} > 0$. It is noteworthy that the elastic constants of both C_6 and C_{10} clathrates satisfy the Born criteria, ensuring the positive definiteness of the elastic tensor and robust mechanical stability. Building upon the elucidated elastic constants, we proceed to calculate several polycrystalline elastic moduli, including bulk modules (B), shear modulus (G), Young's moduli (E), Poisson's ratio (ν), Pugh's ratio (B/G), anisotropy index (A^U), and Vickers hardness (H_v). A detailed discussion along with the three-dimensional visualizations of Young's modulus and shear modulus is presented in Fig. S6 [37]. Notably, the value of B surpasses that of G, indicating that B is the predominant parameter influencing the mechanical stability of both clathrates. Furthermore, the Pugh crystal mechanics standard [62] illustrates that materials with $B/G < 1.75$ or $\nu < 0.26$ are typically classified as brittle ones [63]. For both carbon clathrates, the values of B/G and ν satisfy this standard, indicating their brittle nature.

Moreover, high bulk modulus ($B > 300$ GPa) contributes significantly to surface damage resistance. Naturally

TABLE I. Calculated lattice parameters a (Å), bond length d (Å), elastic constants C_{ij}, bulk modulus B, shear modulus G, Young's moduli E, Poisson's ratio ν, Pugh ratio B/G, anisopy index A^U, and Vickers hardness H_v (GPa) of pristine C_6 and C_{10} clathrates.

	a	d_1	d_2	C_{11}	C_{12}	C_{44}	B	G	E	ν	B/G	A^U	H_v
C_6	4.38	1.55	—	807.32	101.06	302.48	336.48	321.82	732.06	0.14	1.05	0.03	52.54
C_{10}	6.69	1.58	1.54	575.75	164.16	319.19	301.36	267.69	619.61	0.16	1.13	0.23	44.28

occurring minerals, renowned for their hardness, such as alumina (Al_2O_3) and silicon carbide (SiC) [64], possess notably high bulk moduli, indicating their resistance to compression (i.e., they are quite incompressible). Superhard materials ($H_v > 40$ GPa) [65], such as c-BN and diamond [64], exhibit even higher bulk modulus values ($B > 400$ GPa). In the investigated C_6 and C_{10} clathrates, the bulk modules are found to be 336.48 and 301.36 GPa, respectively. However, it is worth noting that while all superhard materials are ultra-incompressible, not all ultra-incompressible materials are superhard. The hardness of the materials can be evaluated by using Vickers hardness (H_v). Employing the empirical model $H_v = 2.0(k^2G)^{0.585} - 3.0$ [66], in which $k = G/B$, the Vickers hardness of C_6 and C_{10} clathrates is calculated to be 52.54 and 44.28 GPa, respectively. These values surpass those of traditional hard covalent materials such as WB_4 ($H_v = 43$ GPa) [67,68], B_4C ($H_v = 30$ GPa) [64], SiC ($H_v = 28$ GPa), Al_2O_3 ($H_v = 22$ GPa), etc. Hence, the predicted C_6 and C_{10} clathrates can be classified as superhard materials.

B. Electronic structure

Figure 3 illustrates the calculated orbital-resolved band structure, electronic density of states (DOS) as well as the orbital-projected DOS (PDOS) of pristine C_6 and C_{10}
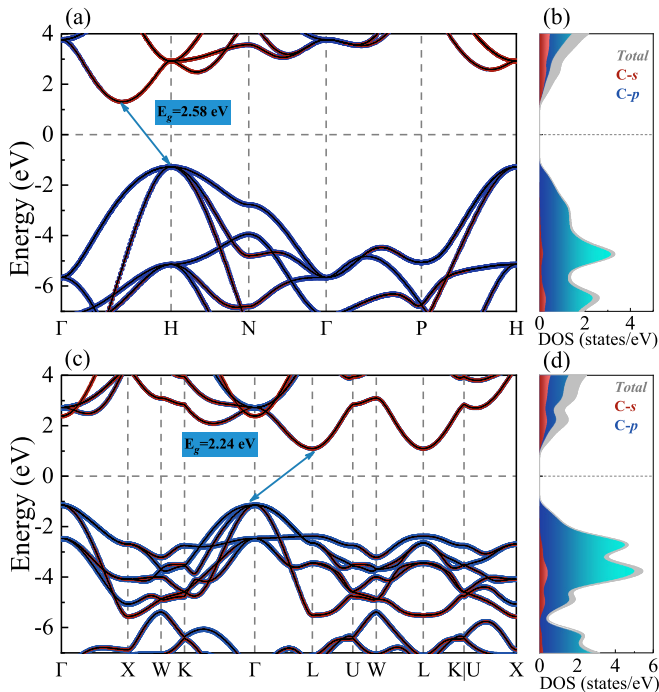
FIG. 3. Orbital-resolved band structures, total and orbital-resolved DOS of pristine C_6 (a, b) and C_{10} (c, d) clathrates.

clathrates along the high-symmetry directions in the first Brillouin zone (BZ). As evidenced by the results, both pristine carbon clathrates exhibit inherent insulating properties, characterized by an indirect bandgap of 2.58 and 2.24 eV, respectively. It is worth emphasizing that the Perdew-Burke-Ernzerhof (PBE) parameterized generalized gradient approximation (GGA) [69,70] typically tends to underestimate the bandgap, implying that the actual bandgap should be greater. The fully occupied valence band below the Fermi level is predominantly governed by the sp^3-hybridized σ-bonding bands. Interestingly, several saddle points are observed around the high-symmetry point below the Fermi level, particularly in C_{10}. Furthermore, the band dispersion around -3 eV along the high-symmetry K-Γ-L direction in the C_{10} clathrate exhibits small slope, giving rise to a vHs in the DOS. In metallic systems, such localization of electronic states often augments metallic properties and can potentially induce high-T_c superconductivity, since the T_c can be estimated by: $k_BT_c = 1.13\hbar\omega_D e^{-\frac{1}{N(0)V}}$, where $N(0)$ represents the DOS at the Fermi level. Evidently, the T_c can be promoted by the enlarged $N(0)$ [71].

One commonly employed method for regulating the position of Fermi level is carrier doping [72,73]. In the case of these carbon clathrates, it is a best-case scenario for enhancing superconductivity by doping so as to shift the Fermi level. In this work, we utilize a jellium model to simulate the effects of carrier doping by directly manipulating the total electron count of the system. Under hole doping, the Fermi level shifts downward with respect to the pristine systems. Based on the premise of dynamic stability, the maximum doping concentration that C_6 and C_{10} clathrates can achieve is determined to be 9.51×10^{21} and 1.76×10^{22} holes/cm³, respectively. The corresponding band structures and Fermi surfaces (FSs) are depicted in Fig. 4. In these hole-doped carbon systems, the DOS around the E_F is dominated by C-$2p$ orbitals, contributing over 90% for both clathrates. The first-principles band structures are accurately reproduced by interpolating the real-space Hamiltonian generated by maximally localized Wannier functions (MLWFs) [Figs. 7(a) and 7(e)] [27,74]. This attests to the validity of subsequent MLWFs-based interpolation and unequivocally confirms that the partially filled bands are sp^3-hybridized σ-bonding bands. The Fermi level intersects with three partially occupied valence bands, generating three hole pockets centered on H for C_6 and on Γ for C_{10} clathrates, respectively. The innermost pocket exhibits a lighter mass while the outermost pocket displays a heavier mass, as illustrated in Figs. 4(e)–4(j). Noteworthy FS nesting within the first BZ is observed, particularly in C_{10} clathrate, characterized by three mutually contained FSs. The nesting function will be shown later. These features may boost the likelihood of formation of Cooper pairs around the Fermi surface and
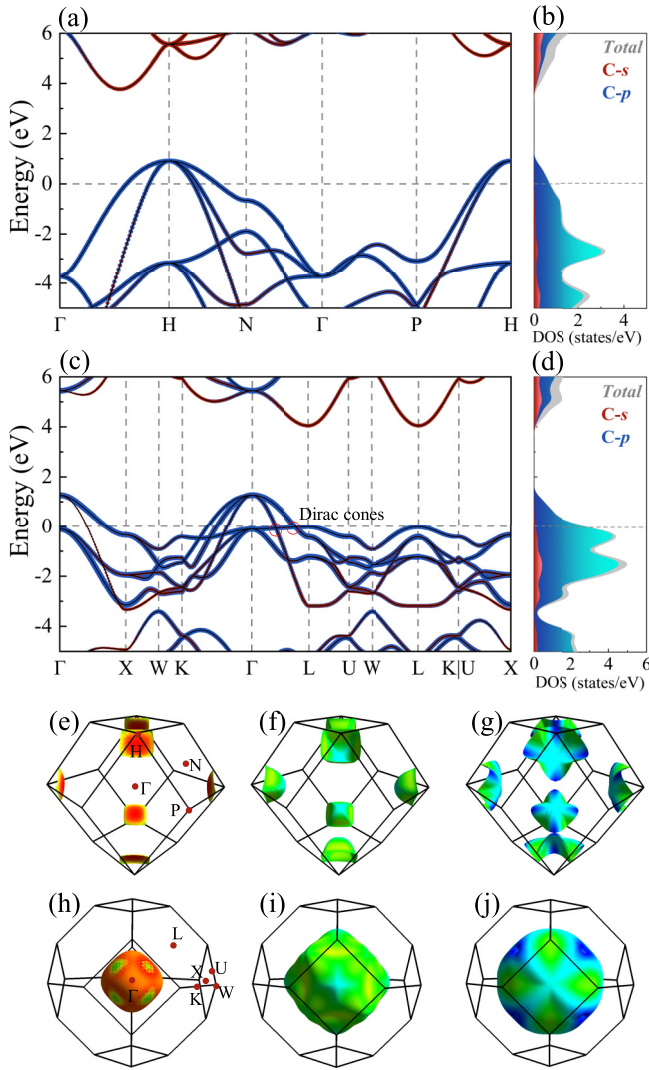
FIG. 4. Orbital-resolved band structure, total and orbital-resolved DOS of hole-doped C_6 (a, b) and C_{10} (c, d) clathrates. Corresponding FSs of hole-doped C_6 (e–g) and C_{10} (h–j) clathrates.

enhance the EPC, thereby fostering the emergence of high-T_c superconductivity [75–77]. Remarkably, for C_{10} clathrate, in the Γ-L direction around the Fermi level, a flat band intersects with two parabolic bands, leading to two tilted Dirac cones and giant DOS [$N(0)$], which are shown in Figs. 4(c) and 4(d). Further elevation of hole-doping levels will result in the partial occupation of such bands, which may closely correlate with lattice instability at higher doping concentrations of C_{10} clathrate.

C. Electron-phonon coupling and superconductivity

With the successful room-pressure metallization of C_6 and C_{10} clathrates achieved through hole doping, we turn attention to investigating their potential superconductivity within the framework of a phonon-mediated mechanism. Figure 5 exhibits the lattice dynamics of hole-doped C_6 and C_{10}, with stabilities confirmed by the absence of imaginary modes in phonon spectra. In doped C_6 [Fig. 5(a)], dispersionless phonon modes observed in the middle and high-frequency
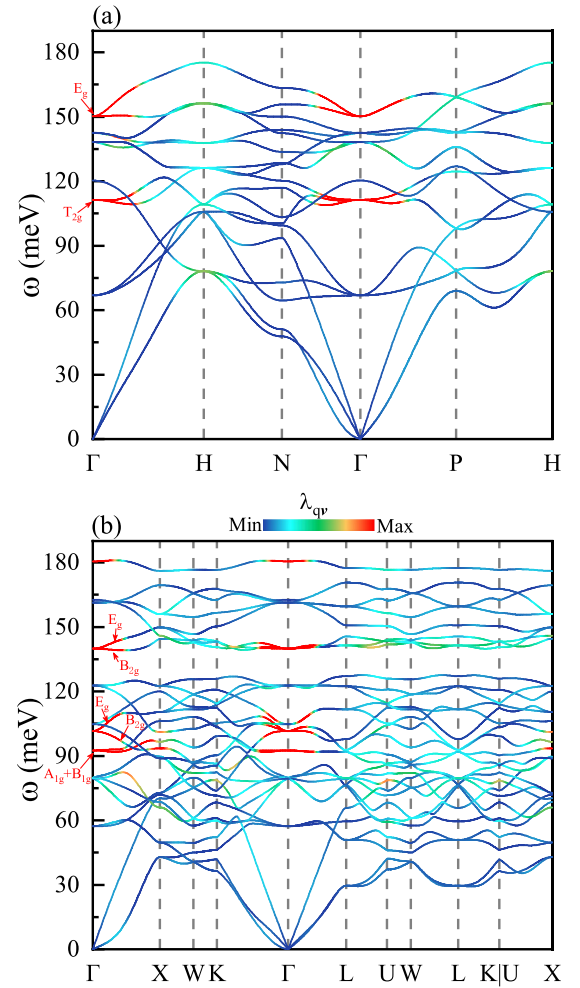
FIG. 5. Phonon spectra with color representation of $\lambda_{\mathbf{q}\nu}$ at the given vectors for hole-doped C_6 (a) and C_{10} (b) clathrates.

regions give rise to multiple peaks in the phonon density of states (PhDOS) [Fig. 6(a)]. While optical modes around the H point display abnormal hardening, the majority of phonon modes exhibit significant softening. Compare with the pristine case, which can be seen in Figs. S4(a) and S4(b) in SM [37]. Notably, the frequency of triple degenerate T_{2g} modes decreases from about 128.4 meV to 111.4 meV, showcasing a strong coupling with σ electrons. Similarly, double degenerate softened E_g modes at the highest frequency also exhibit substantial coupling strength, whereas acoustic modes below 60 meV remain relatively unaffected. As for doped C_{10} [Fig. 5(b)], the overall hardening of the highest optical mode creates a 5.5 meV frequency gap around 173 meV, with a larger gap appearing around 130 meV, exhibiting a gap value about 11.5 meV. The prominent peak in the PhDOS is observed just above the larger gap, owing to dispersionless phonon modes. The primary softened phonon modes are also distinctly identified. Strong EPC between σ electrons and the vibration modes of carbon atoms in the medium and high frequency is evident in both hole-doped C_6 and C_{10}. It is worth mentioning that this feature exhibits similarities with the behavior observed in compressed LaH_{10} [78], in which
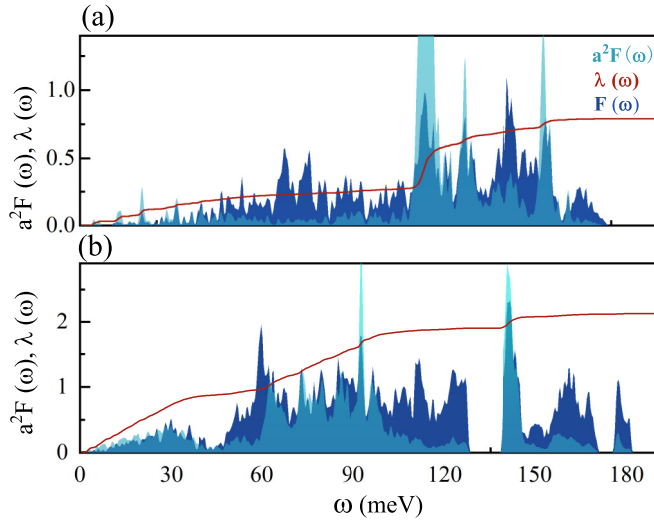
FIG. 6. Phonon DOS $F(\omega)$, Eliashberg spectral function $\alpha^2 F(\omega)$, and accumulated EPC constant $\lambda(\omega)$ for hole-doped C_6 (a) and C_{10} (b) clathrate. For clarity, the graduation of $F(\omega)$ is omitted.

optical phonon modes of H atoms contribute over 80% of the total EPC.

Through MLWFs-based interpolation, the accurate isotropic Eliashberg spectral function $\alpha^2 F(\omega)$ for doped C_6 and C_{10} clathrates are obtained, as depicted in Fig. 6. In the case of C_6 clathrate [Fig. 6(a)], $\alpha^2 F(\omega)$ reveals three main peaks, with the highest peak centered around 113 meV, arising from strongly coupled T_{2g} modes. The tiny proportion

of $\alpha^2 F(\omega)$ below 60 meV indicates that acoustic phonons have weak couplings with electrons, self-consistent with Fig. 5(a), in which the strong-coupled phonons mainly locate above 110 meV. By integrating $\alpha^2 F(\omega)$, we find that the EPC constant λ and logarithmic average frequency $\omega_{\log}$ are equal to 0.76 and 946.18 K, respectively. Utilizing the modified McMillian-Allen-Dynes formula [15] with a typical Coulomb potential μ^* of 0.1 [14,79,80], the T_c of doped C_6 is computed to be $T_c^{MAD} \sim 39$ K, just reaching the McMillan limit. Since the superconducting energy gap $\Delta_{n\mathbf{k}}$ of these carbon-cage-network has never been specifically investigated, we therefore apply the fully isotropic and anisotropic Migdal-Eliashberg equations to investigate the superconducting energy gap. Figures 7(c) and 7(d) are the distribution of the anisotropical EPC strength $\lambda_{\mathbf{k}}$ and the normalized density of the superconducting gap $\Delta_{n\mathbf{k}}$ at each temperature of hole-doped C_6. These distributions suggest a single superconducting energy gap nature since the superconducting density of states (SDOS), relative to the DOS in the normal state $N_s(\omega)/N_N(\omega)$, has only one peak at $\sim$6.9 meV. These results are reasonable because C_6 consists of a single element and there is only σ orbital around the Fermi level, precluding the formation of multiple energy gaps. This characteristic distinguishes it from the well-known multigap MgB_2 [14,81–83], in which the σ and π orbitals lead to separate superconducting gaps. The temperature at which $\Delta_{n\mathbf{k}}$ closes corresponds to the superconducting transition temperature, which is determined to be $T_c^{Aniso} \sim 43$ K, surpassing that of MgB_2 and the above-mentioned alkali metal doped C_{60}. Additionally, the transition temperature obtained
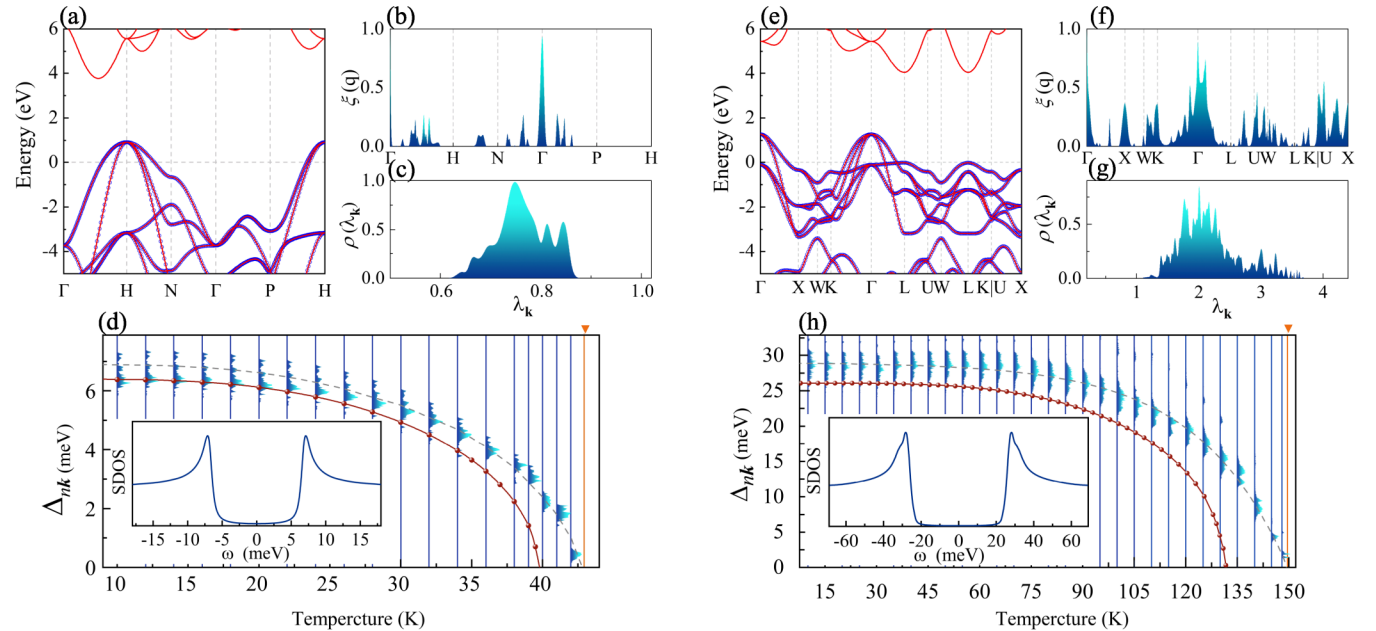
FIG. 7. Band structures of hole-doped C_6 (a) and C_{10} (e) clathrates; the red and blue lines denote the bands obtained by the first-principles calculation and interpolated by the real-space Hamiltonian, respectively. The Fermi level is set to zero. (b, f) FS nesting function $\xi(\mathbf{q})$. (c, g) The normalized distribution of the EPC strength $\lambda_{\mathbf{k}}$, revealing their strong anisotropy. (d, h) Energy distribution of the isotropic (red) and anisotropic (blue) superconducting gap $\Delta_{n\mathbf{k}}$ as a function of temperature. The insets are the SDOS under a low temperature of 10 K for hole-doped C_6 and C_{10} clathrates. The orange line signifies the temperature threshold at which energy gaps close, whereas the gray dashed lines are guides to the eye.

TABLE II. Calculated superconducting properties of hole-doped C_6 and C_{10} clathrate, including data of doping concentration n (holes/cm^3), $N(E_F)$ (states/spin/Ry/unit cell), logarithmically averaged phonon frequency $\omega_{\log}$ (K), total EPC constant λ, Sommerfeld constant γ ($\frac{mJ}{mol \cdot K^2}$), specific heat jump $\Delta C(T_c)$ ($\frac{mJ}{mol \cdot K^2}$), critical magnetic field $H_c(0)$ (T), isotope coefficient β, $\frac{2\Delta(0)}{k_B T_c}$, superconducting T_cs determined by simultaneously solving the semiempirical McMillian-Allen-Dynes formula ($T_{c,0.1}^{MAD}$), isotropic ($T_{c,0.1}^{Iso}$), and anisotropic Migdal-Eliashberg equations ($T_{c,0.1}^{Aniso}$) when setting the Coulomb pseudopotential μ^* to a typical value of 0.1.

	n	$N(E_F)$	λ	$\omega_{\log}$	γ	$\Delta C(T_c)$	$H_c(0)$	β	$\frac{2\Delta(0)}{k_B T_c}$	$T_{c,0.1}^{MAD}$	$T_{c,0.1}^{Iso}$	$T_{c,0.1}^{Aniso}$
C_6	9.51×10^{21}	4.75	0.76	940.89	0.12	0.21	0.34	0.46	3.72	39.20	39.97	43.05
C_{10}	1.76×10^{22}	17.95	2.23	593.43	0.51	1.51	2.36	0.49	5.13	117.77	131.78	149.69

by solving the isotropic Migdal-Eliashberg equations is estimated to be $T_c^{Iso} \sim 40$ K (red line). This is together with the result from the McMillian-Allen-Dynes formula, exhibiting varying degrees of underestimation of T_c, attributed to the strong anisotropy revealed by the electronic structure and normalized distribution of the EPC strength λ_{nk}.

For hole-doped C_{10} clathrate, compared with the pristine case, a greater number of phonon modes located at the middle frequency around the Γ point undergo significant softening, as presented in Figs. S4(c) and S4(d). By integrating $\alpha^2 F(\omega)$, we find that the EPC constant λ and logarithmic average frequency $\omega_{\log}$ are equal to 2.23 and 592.02 K, respectively. Given that the total EPC constant λ is larger than 1.50, the full Allen-Dynes formula [84] is deemed more appropriate for evaluating its transition temperature. The calculated strong-coupling correction factor and the shape correction factor are $f_1 = 1.15$ and $f_2 = 1.12$, respectively. Consequently, with a typical Coulomb potential μ^* of 0.1, the T_c of hole-doped C_{10} is determined to be $T_c^{MAD} \sim 118$ K. Similar to hole-doped C_6, by solving the fully anisotropic Migdal-Eliashberg equations, as depicted in Figs. 7(g) and 7(h), it can be found that hole-doped C_{10} clathrate also exhibits characteristics of a single-gap superconductor, with the maximum normalized density of the superconducting gap $\Delta_{nk} \sim 28.26$ meV. Such a big gap contributes to a high superconducting transition temperature, which is determined to be $T_c^{Aniso} \sim 150$ K, about 27% and 14% higher than that of the Allen-Dynes ($T_c^{MAD} \sim 118$ K) and isotropic results ($T_c^{Iso} \sim 132$ K, red line), respectively. Furthermore, upon comparison with the highest T_c of 116 K observed in carbon cages doped with alkali or alkaline earth metals as reported by previous researchers [85,86], we discern that valence band metallization is more conducive to superconductivity than conduction band metallization.

Additionally, to better elucidate the origin of the obtained high T_c, we conducted further calculations of the FS nesting function $\xi(\mathbf{q})$ in the first BZ along the high-symmetry path [87–89], with the results depicted in Figs. 7(b) and 7(f). The nesting function $\xi(\mathbf{q})$ can be directly evaluated by calculating the imaginary part of the bare electronic susceptibility. $\xi(\mathbf{q})$ is defined as $\sum_{nm\mathbf{k}} \delta(\epsilon_\mathbf{k}^n - \epsilon_F)\delta(\epsilon_{\mathbf{k+q}}^m - \epsilon_F)$, in which n and m are the indices of energy bands, $\epsilon_\mathbf{k}^n$ and $\epsilon_{\mathbf{k+q}}^m$ represent the eigenvalues of the electronic states with respect to the Fermi energy, and ϵ_F is the Fermi energy. For clarity, $\xi(\mathbf{q})$ is normalized by $\xi(\Gamma)$, because Γ point always possesses the strongest nesting. Since the entire FS nests into itself, there is no actual physical meaning for $\xi(\Gamma)$. The results indicate that the nesting throughout the entire BZ of hole-doped C_{10} clathrate is significantly broader and stronger compared with that of C_6. Moreover, those positions of optical phonons

exhibiting large $\lambda_{\mathbf{q}\nu}$ in Fig. 5 align closely with the peaks of the nesting function, especially in C_{10} clathrate. Therefore, we consider that the enhancement of the nesting effect induced by doping accounts for the origin of the softened phonons with large $\lambda_{\mathbf{q}\nu}$.

Apart from the opening of energy gaps on the FS when the materials transition into a superconducting state, several key phenomena are commonly employed to characterize the fundamental properties of conventional superconductors, both theoretically and experimentally. These include the specific heat jump at T_c [79,83,90], Meissner effect [79], and isotope effect. The above phenomena can be elucidated by calculating the specific heat jump coefficient $\Delta C(T_c)$, critical magnetic field $H_c(0)$, and isotope coefficient β, with the results presented in Table II. It is noteworthy that the obtained $2\Delta(0)/k_B T_c$ and isotope coefficient β of hole-doped C_6 clathrate are 3.72 and 0.46, respectively, while for C_{10} they are 5.13 and 0.49, which are close to the values given by conventional BCS theory ($2\Delta(0)/k_B T_c \sim 3.53$, $\beta \sim 0.50$), further confirming that both hole-doped C_6 and C_{10} clathrates are conventional phonon-mediated superconductors. Moreover, the calculated superconducting parameters can serve as reference data for potential experimental verification in the future.

D. Discussion

Before concluding, we would like to discuss the potential experimental synthesis of C_6 and C_{10} clathrates. We have systematically examined the formation enthalpies of these carbon clathrates at ambient conditions as well as under pressure. The enthalpy differences curves relative to several experimentally synthesizable structures at pressures are exhibited in Fig. S5 [37]. Although C_6 and C_{10} phases invariably possess higher enthalpies than diamond and elemental carbon phases, indicating their metastable nature, their enthalpies are lower than those of the T-carbon [91] and graphite under ambient pressure, which provides the possibility for the experimental synthesis of these carbon clathrates.

To achieve the highest T_c of these carbon clathrates, the introduction of hole doping is essential. Boron has one less electron than carbon, and due to its small atomic radius, boron is relatively easily incorporated into diamond. As boron acts as a charge acceptor, the resulting diamond is effectively hole-doped [92–95]. To further elucidate the realization of hole doping in C_6 and C_{10} clathrates, we perform the B doping on these two carbon clathrates to simulate the hole-doping effect. We find that for C_6 and C_{10}, when the B-doping concentration falls within the ranges of 4.2%–6.3% and 15.0%–16.2%,

respectively, the achieved DOS around the Fermi level is almost similar as the direct hole-doping cases (Fig. S7) [37]. From the calculated DOS it can be observed that the shift of the Fermi energy increases with the B concentration, and the introduction of B does not induce evident midgap states, but leads to an almost rigid shift of the Fermi energy into the valence band, indicating effective p-type doping. Additionally, the adopted concentration of B is similar to that of the B-doped diamond [93–95] ($\sim$5% B concentration) and lower than that of amorphous quenched carbon ($\sim$17% B concentration) fabricated in experiments [96], indicating these concentrations are relatively moderate and achievable. Detailed results can be found in SM [37].

III. CONCLUSION

In summery, through the substitution of elements in experimentally synthesized materials, we have devised two pure carbon-cage-network structures, C_6 and C_{10}, and systematically elucidated their lattice dynamics, mechanical properties, electronic structure, and EPC properties via first-principles calculations. The results reveal that both pristine C_6 and C_{10} manifest insulating behavior while concurrently exhibiting ultra-high hardness. By shifting the Fermi level through hole doping, we have successfully obtained the metallized sp^3-hybridized σ-bonding bands in both structures. The EPC strength λ has been accurately determined to be 0.76 and 2.23, respectively. We find that the strong coupling between σ electrons and softened phonon modes facilitates the formation of high-T_c states. By taking the anisotropy of electronic properties into consideration, solving the anisotropic Migdal-Eliashberg equations, the superconducting transition temperatures are determined to be approximately 43 K and 150 K for hole-doped C_6 and C_{10} clathrates, respectively. Thus, these two compounds are ambient pressure phonon-mediated high-T_c superconductors. This study emphasizes the potential of carbon-cage-network materials as a promising avenue for exploring substances that exhibit both high-temperature superconductivity and ultra-high hardness simultaneously.

[1] D. Duan, Y. Liu, F. Tian, D. Li, X. Huang, Z. Zhao, H. Yu, B. Liu, W. Tian, and T. Cui, Pressure-induced metallization of dense $(H_2S)_2H_2$ with high-T_c superconductivity, Sci. Rep. **4**, 6968 (2014).

[2] A. P. Drozdov, M. I. Eremets, I. A. Troyan, V. Ksenofontov, and S. I. Shylin, Conventional superconductivity at 203 kelvin at high pressures in the sulfur hydride system, Nature (London) **525**, 73 (2015).

[3] L. P. Gor'kov and V. Z. Kresin, *Colloquium*: High pressure and road to room temperature superconductivity, Rev. Mod. Phys. **90**, 011001 (2018).

[4] H. Wang, J. S. Tse, K. Tanaka, T. Iitaka, and Y. Ma, Superconductive sodalite-like clathrate calcium hydride at high pressures, Proc. Natl. Acad. Sci. USA **109**, 6463 (2012).

[5] L. Ma, K. Wang, Y. Xie, X. Yang, Y. Wang, M. Zhou, H. Liu, X. Yu, Y. Zhao, H. Wang *et al.*, High-temperature superconducting phase in clathrate calcium hydride CaH_6 up to 215 K at a pressure of 172 GPa, Phys. Rev. Lett. **128**, 167001 (2022).

[6] Y. Li, J. Hao, H. Liu, J. S. Tse, Y. Wang, and Y. Ma, Pressure-stabilized superconductive yttrium hydrides, Sci. Rep. **5**, 9948 (2015).

[7] I. A. Troyan, D. V. Semenok, A. G. Kvashnin, A. V. Sadakov, O. A. Sobolevskiy, V. M. Pudalov, A. G. Ivanova, V. B. Prakapenka, E. Greenberg, A. G. Gavriliuk *et al.*, Anomalous high-temperature superconductivity in YH_6, Adv. Mater. **33**, 2006832 (2021).

[8] F. Peng, Y. Sun, C. J. Pickard, R. J. Needs, Q. Wu, and Y. Ma, Hydrogen clathrate structures in rare earth hydrides at high pressures: Possible route to room-temperature superconductivity, Phys. Rev. Lett. **119**, 107001 (2017).

[9] H. Liu, I. I. Naumov, R. Hoffmann, N. Ashcroft, and R. J. Hemley, Potential high-T_c superconducting lanthanum and yttrium hydrides at high pressure, Proc. Natl. Acad. Sci. USA **114**, 6990 (2017).

[10] M. Somayazulu, M. Ahart, A. K. Mishra, Z. M. Geballe, M. Baldini, Y. Meng, V. V. Struzhkin, and R. J. Hemley, Evidence for superconductivity above 260 K in lanthanum superhydride at megabar pressures, Phys. Rev. Lett. **122**, 027001 (2019).

[11] A. Drozdov, P. Kong, V. Minkov, S. Besedin, M. Kuzovnikov, S. Mozaffari, L. Balicas, F. Balakirev, D. Graf, V. Prakapenka *et al.*, Superconductivity at 250 K in lanthanum hydride under high pressures, Nature (London) **569**, 528 (2019).

[12] W. Chen, D. V. Semenok, X. Huang, H. Shu, X. Li, D. Duan, T. Cui, and A. R. Oganov, High-temperature superconducting phases in cerium superhydride with a T_c up to 115 K below a pressure of 1 megabar, Phys. Rev. Lett. **127**, 117001 (2021).

[13] J. Bardeen, L. N. Cooper, and J. R. Schrieffer, Theory of superconductivity, Phys. Rev. **108**, 1175 (1957).

[14] E. R. Margine and F. Giustino, Anisotropic Migdal-Eliashberg theory using Wannier functions, Phys. Rev. B **87**, 024505 (2013).

[15] P. B. Allen and R. C. Dynes, Transition temperature of strong-coupled superconductors reanalyzed, Phys. Rev. B **12**, 905 (1975).

[16] H. W. Kroto, J. R. Heath, S. C. O'Brien, R. F. Curl, and R. E. Smalley, C_{60}: Buckminsterfullerene, Nature (London) **318**, 162 (1985).

[17] W. Krätschmer, L. D. Lamb, K. Fostiropoulos, and D. R. Huffman, Solid C_{60}: A new form of carbon, Nature (London) **347**, 354 (1990).

[18] A. Hebard, M. Rosseinsky, R. Haddon, D. Murphy, S. H. Glarum, T. Palstra, A. Ramirez, and A. Kortan, Superconductivity at 18 K in potassium-doped C_{60}, Nature (London) **350**, 600 (1991).

[19] K. Tanigaki, T. Ebbesen, S. Saito, J. Mizuki, J. Tsai, Y. Kubo, and S. Kuroshima, Superconductivity at 33 K in $Cs_xRb_yC_{60}$, Nature (London) **352**, 222 (1991).

[20] T. Palstra, O. Zhou, Y. Iwasa, P. Sulewski, R. Fleming, and B. Zegarski, Superconductivity at 40 K in cesium doped C_{60}, Solid State Commun. **93**, 327 (1995).

[21] I. Spagnolatti, M. Bernasconi, and G. Benedek, Electron-phonon interaction in the solid form of the smallest fullerene C_{20}, Europhys. Lett. **59**, 572 (2002).

[22] F. Zipoli, M. Bernasconi, and G. Benedek, Electron-phonon coupling in halogen-doped carbon clathrates from first principles, Phys. Rev. B **74**, 205408 (2006).

[23] S. Di Cataldo, S. Qulaghasi, G. B. Bachelet, and L. Boeri, High-T_c superconductivity in doped boron-carbon clathrates, Phys. Rev. B **105**, 064516 (2022).

[24] J.-N. Wang, X.-W. Yan, and M. Gao, High-temperature superconductivity in SrB_3C_3 and BaB_3C_3 predicted from first-principles anisotropic Migdal-Eliashberg theory, Phys. Rev. B **103**, 144515 (2021).

[25] P. Zhang, X. Li, X. Yang, H. Wang, Y. Yao, and H. Liu, Path to high-T_c superconductivity via Rb substitution of guest metal atoms in the SrB_3C_3 clathrate, Phys. Rev. B **105**, 094503 (2022).

[26] F. Giustino, M. L. Cohen, and S. G. Louie, Electron-phonon interaction using Wannier functions, Phys. Rev. B **76**, 165108 (2007).

[27] A. A. Mostofi, J. R. Yates, Y.-S. Lee, I. Souza, D. Vanderbilt, and N. Marzari, Wannier90: A tool for obtaining maximally-localised Wannier functions, Comput. Phys. Commun. **178**, 685 (2008).

[28] S. Poncé, E. Margine, C. Verdi, and F. Giustino, EPW: Electron–phonon coupling, transport and superconducting properties using maximally localized Wannier functions, Comput. Phys. Commun. **209**, 116 (2016).

[29] F. Giustino, Electron-phonon interactions from first principles, Rev. Mod. Phys. **89**, 015003 (2017).

[30] T.-T. Gai, P.-J. Guo, H.-C. Yang, Y. Gao, M. Gao, and Z.-Y. Lu, Van Hove singularity induced phonon-mediated superconductivity above 77 K in hole-doped SrB_3C_3, Phys. Rev. B **105**, 224514 (2022).

[31] M. Gao, X.-W. Yan, Z.-Y. Lu, and T. Xiang, Phonon-mediated high-temperature superconductivity in the ternary borohydride KB_2H_8 under pressure near 12 GPa, Phys. Rev. B **104**, L100504 (2021).

[32] Y. Zhao, C. Lian, S. Zeng, Z. Dai, S. Meng, and J. Ni, Two-gap and three-gap superconductivity in AlB_2-based films, Phys. Rev. B **100**, 094516 (2019).

[33] L. Liu, X. Liu, P. Song, L. Zhang, X. Huang, W. Zhang, Z. Zhang, and Y. Jia, Surface superconductivity with high transition temperatures in layered $Ca_nB_{n+1}C_{n+1}$ Films, Nano Lett. **23**, 1924 (2023).

[34] W. H. Bragg and W. L. Bragg, The structure of the diamond, Nature (London) **91**, 557 (1913).

[35] A. K. Geim, Graphene: Status and prospects, Science **324**, 1530 (2009).

[36] A. R. Oganov, J. Chen, C. Gatti, Y. Ma, Y. Ma, C. W. Glass, Z. Liu, T. Yu, O. O. Kurakevych, and V. L. Solozhenko, Ionic high-pressure form of elemental boron, Nature (London) **457**, 863 (2009).

[37] See Supplemental Material at http://link.aps.org/supplemental/10.1103/PhysRevB.110.104504 for computational details, converge test of superconducting energy gaps, electron localization function (ELF), charge density difference, and crystal orbital Hamiltonian population (COHP) of pristine C_6 and C_{10} clathrates, phonon dispersion before and after doping, the possibility of experimental synthesis, mechanical properties, the realization of hole-doping by boron-doping in C_6 and C_{10} clathrates, and the structural information of clathrate structures, and which includes Refs. [38–58].

[38] W. Kohn, A. D. Becke, and R. G. Parr, Density functional theory of electronic structure, J. Phys. Chem. **100**, 12974 (1996).

[39] P. Giannozzi, S. Baroni, N. Bonini, M. Calandra, R. Car, C. Cavazzoni, D. Ceresoli, G. L. Chiarotti, M. Cococcioni, I. Dabo *et al.*, QUANTUM ESPRESSO: A modular and open-source software project for quantum simulations of materials, J. Phys.: Condens. Matter **21**, 395502 (2009).

[40] P. Giannozzi, O. Baseggio, P. Bonfá, D. Brunato, R. Car, I. Carnimeo, C. Cavazzoni, S. de Gironcoli, P. Delugas, F. Ferrari Ruffino *et al.*, Quantum ESPRESSO toward the exascale, J. Chem. Phys. **152**, 154105 (2020).

[41] M. Schlipf and F. Gygi, Optimization algorithm for the generation of ONCV pseudopotentials, Comput. Phys. Commun. **196**, 36 (2015).

[42] P. E. Blöchl, Projector augmented-wave method, Phys. Rev. B **50**, 17953 (1994).

[43] S. Baroni, S. de Gironcoli, A. Dal Corso, and P. Giannozzi, Phonons and related crystal properties from density-functional perturbation theory, Rev. Mod. Phys. **73**, 515 (2001).

[44] J. Noffsinger, F. Giustino, B. D. Malone, C.-H. Park, S. G. Louie, and M. L. Cohen, EPW: A program for calculating the electron–phonon coupling using maximally localized Wannier functions, Comput. Phys. Commun. **181**, 2140 (2010).

[45] G. Kresse and J. Furthmüller, Efficient iterative schemes for *ab initio* total-energy calculations using a plane-wave basis set, Phys. Rev. B **54**, 11169 (1996).

[46] R. Dynes, McMillan's equation and the T_c of superconductors, Solid State Commun. **10**, 615 (1972).

[47] I. Hamada, van der Waals density functional made accurate, Phys. Rev. B **89**, 121103(R) (2014).

[48] K. Lee, E. D. Murray, L. Kong, B. I. Lundqvist, and D. C. Langreth, Higher-accuracy van der Waals density functional, Phys. Rev. B **82**, 081101(R) (2010).

[49] A. Jain, S. P. Ong, G. Hautier, W. Chen, W. D. Richards, S. Dacek, S. Cholia, D. Gunter, D. Skinner, G. Ceder, and K. A. Persson, Commentary: The Materials Project: A materials genome approach to accelerating materials innovation, APL Mater. **1**, 011002 (2013).

[50] L. Zhu, G. M. Borstad, H. Liu, P. A. Guńka, M. Guerette, J.-A. Dolyniuk, Y. Meng, E. Greenberg, V. B. Prakapenka, B. L. Chaloux *et al.*, Carbon-boron clathrates as a new class of sp^3-bonded framework materials, Sci. Adv. **6**, eaay8361 (2020).

[51] L. Hou, X. Cui, B. Guan, S. Wang, R. Li, Y. Liu, D. Zhu, and J. Zheng, Synthesis of a monolayer fullerene network, Nature (London) **606**, 507 (2022).

[52] C. Jiang, S. G. Srinivasan, A. Caro, and S. A. Maloy, Structural, elastic, and electronic properties of Fe_3C from first principles, J. Appl. Phys. **103**, 043502 (2008).

[53] S. Li, X. Ju, and C. Wan, Theoretical studies of elastic properties of orthorhombic $LiBH_4$, Comput. Mater. Sci. **81**, 378 (2014).

[54] E. Cadelano, P. L. Palla, S. Giordano, and L. Colombo, Elastic properties of hydrogenated graphene, Phys. Rev. B **82**, 235414 (2010).

[55] Y. Le Page and P. Saxe, Symmetry-general least-squares extraction of elastic data for strained materials from *ab initio* calculations of stress, Phys. Rev. B **65**, 104104 (2002).

[56] E. Schreiber, O. L. Anderson, N. Soga, and J. F. Bell, Elastic constants and their measurement, J. Appl. Mech. **42**, 747 (1975).

[57] R. Hill, The elastic behaviour of a crystalline aggregate, Proc. Phys. Soc. A **65**, 349 (1952).

[58] S. I. Ranganathan and M. Ostoja-Starzewski, Universal elastic anisotropy index, Phys. Rev. Lett. **101**, 055504 (2008).

[59] A. D. Becke and K. Edgecombe, A simple measure of electron localization in atomic and molecular-systems, J. Chem. Phys. **92**, 5397 (1990).

[60] R. Dronskowski and P. E. Bloechl, Crystal orbital Hamilton populations (COHP): Energy-resolved visualization of chemical bonding in solids based on density-functional calculations, J. Phys. Chem. **97**, 8617 (1993).

[61] F. Mouhat and F. X. Coudert, Necessary and sufficient elastic stability conditions in various crystal systems, Phys. Rev. B **90**, 224104 (2014).

[62] S. F. Pugh, XCII. Relations between the elastic moduli and the plastic properties of polycrystalline pure metals, Philos. Mag. **45**, 823 (1954).

[63] T. Sōma, A. Sawaoka, and S. Saito, Characterization of wurtzite type boron nitride synthesized by shock compression, Mater. Res. Bull. **9**, 755 (1974).

[64] D. M. Teter, Computational alchemy: The search for new superhard materials, Mater. Res. Bull. **23**, 22 (1998).

[65] M. T. Yeung, R. Mohammadi, and R. B. Kaner, Ultraincompressible, superhard materials, Annu. Rev. Mater. Res. **46**, 465 (2016).

[66] X.-Q. Chen, H. Niu, D. Li, and Y. Li, Modeling hardness of polycrystalline materials and bulk metallic glasses, Intermetallics **19**, 1275 (2011).

[67] Q. Gu, G. Krauss, and W. Steurer, Transition metal borides: Superhard versus ultra-incompressible, Adv. Mater. **20**, 3620 (2008).

[68] R. Mohammadi, A. T. Lech, M. Xie, B. E. Weaver, M. T. Yeung, S. H. Tolbert, and R. B. Kaner, Tungsten tetraboride, an inexpensive superhard material, Proc. Natl. Acad. Sci. USA **108**, 10958 (2011).

[69] J. P. Perdew, K. Burke, and M. Ernzerhof, Generalized gradient approximation made simple, Phys. Rev. Lett. **77**, 3865 (1996).

[70] D. R. Hamann, Optimized norm-conserving Vanderbilt pseudopotentials, Phys. Rev. B **88**, 085117 (2013).

[71] I. Errea, M. Calandra, C. J. Pickard, J. Nelson, R. J. Needs, Y. Li, H. Liu, Y. Zhang, Y. Ma, and F. Mauri, High-pressure hydrogen sulfide from first principles: A strongly anharmonic phonon-mediated superconductor, Phys. Rev. Lett. **114**, 157004 (2015).

[72] B. Uchoa and A. H. Castro Neto, Superconducting states of pure and doped graphene, Phys. Rev. Lett. **98**, 146801 (2007).

[73] L. Boeri, J. Kortus, and O. K. Andersen, Three-dimensional MgB_2-type superconductivity in hole-doped diamond, Phys. Rev. Lett. **93**, 237002 (2004).

[74] G. Pizzi, V. Vitale, R. Arita, S. Blügel, F. Freimuth, G. Géranton, M. Gibertini, D. Gresch, C. Johnson, T. Koretsune *et al.*, Wannier90 as a community code: New features and applications, J. Phys.: Condens. Matter **32**, 165902 (2020).

[75] P.-F. Liu, F. Zheng, J. Li, J.-G. Si, L. Wei, J. Zhang, and B.-T. Wang, Two-gap superconductivity in a Janus MoSH monolayer, Phys. Rev. B **105**, 245420 (2022).

[76] C. Tian, Y. He, Y.-H. Zhu, J. Du, S.-M. Liu, W.-H. Guo, H.-X. Zhong, J. Lu, X. Wang, and J.-J. Shi, Few-hydrogen metal-bonded perovskite superconductor $MgHCu_3$ with a critical temperature of 42 K under atmospheric pressure, Adv. Funct. Mater. **34**, 2304919 (2024).

[77] Y. He and J.-J. Shi, Few-hydrogen high-T_c superconductivity in $(Be_4)_2H$ nanosuperlattice with promising ductility under ambient pressure, Nano Lett. **23**, 8126 (2023).

[78] L. Liu, C. Wang, S. Yi, K. W. Kim, J. Kim, and J.-H. Cho, Microscopic mechanism of room-temperature superconductivity in compressed LaH_{10}, Phys. Rev. B **99**, 140501(R) (2019).

[79] J. P. Carbotte, Properties of boson-exchange superconductors, Rev. Mod. Phys. **62**, 1027 (1990).

[80] P. B. Allen and B. Mitrović, Theory of superconducting T_c, Solid State Phys. **37**, 1 (1983).

[81] Y. Kong, O. V. Dolgov, O. Jepsen, and O. K. Andersen, Electron-phonon interaction in the normal and superconducting states of MgB_2, Phys. Rev. B **64**, 020501(R) (2001).

[82] H. J. Choi, D. Roundy, H. Sun, M. L. Cohen, and S. G. Louie, The origin of the anomalous superconducting properties of MgB_2, Nature (London) **418**, 758 (2002).

[83] H. J. Choi, M. L. Cohen, and S. G. Louie, Anisotropic Eliashberg theory of MgB_2:T_c, isotope effects, superconducting energy gaps, quasiparticles, and specific heat, Physica C **385**, 66 (2003).

[84] W. L. McMillan, Transition temperature of strong-coupled superconductors, Phys. Rev. **167**, 331 (1968).

[85] Y.-L. Hai, M.-J. Jiang, H.-L. Tian, G.-H. Zhong, W.-J. Li, C.-L. Yang, X.-J. Chen, and H.-Q. Lin, Superconductivity above 100 K predicted in carbon-cage network, Adv. Sci. **10**, 2303639 (2023).

[86] S. Lu, H. Liu, I. I. Naumov, S. Meng, Y. Li, J. S. Tse, B. Yang, and R. J. Hemley, Superconductivity in dense carbon-based materials, Phys. Rev. B **93**, 104509 (2016).

[87] M. Calandra and F. Mauri, Charge-density wave and superconducting dome in $TiSe_2$ from electron-phonon interaction, Phys. Rev. Lett. **106**, 196406 (2011).

[88] H. L. Zhuang, M. D. Johannes, A. K. Singh, and R. G. Hennig, Doping-controlled phase transitions in single-layer MoS_2, Phys. Rev. B **96**, 165305 (2017).

[89] J. G. Si, W. J. Lu, H. Y. Wu, H. Y. Lv, X. Liang, Q. J. Li, and Y. P. Sun, Origin of the multiple charge

density wave order in $1T$-VSe$_2$, Phys. Rev. B **101**, 235405 (2020).

[90] J. Bardeen and M. Stephen, Free-energy difference between normal and superconducting states, Phys. Rev. **136**, A1485 (1964).

[91] X.-L. Sheng, Q.-B. Yan, F. Ye, Q.-R. Zheng, and G. Su, T-carbon: A novel carbon allotrope, Phys. Rev. Lett. **106**, 155703 (2011).

[92] R. Kalish, The search for donors in diamond, Diam. Relat. Mater. **10**, 1749 (2001).

[93] Y. Takano, M. Nagao, I. Sakaguchi, M. Tachiki, T. Hatano, K. Kobayashi, H. Umezawa, and H. Kawarada, Superconductivity

in diamond thin films well above liquid helium temperature, Appl. Phys. Lett. **85**, 2851 (2004).

[94] E. A. Ekimov, V. A. Sidorov, E. D. Bauer, N. N. Mel'nik, N. J. Curro, J. D. Thompson, and S. M. Stishov, Superconductivity in diamond, Nature (London) **428**, 542 (2004).

[95] Y. Takano, T. Takenouchi, S. Ishii, S. Ueda, T. Okutsu, I. Sakaguchi, H. Umezawa, H. Kawarada, and M. Tachiki, Superconducting properties of homoepitaxial CVD diamond, Diam. Relat. Mater. **16**, 911 (2007).

[96] A. Bhaumik, R. Sachan, and J. Narayan, High-temperature superconductivity in boron-doped Q-carbon, ACS Nano **11**, 5351 (2017).